energies

MDPI

Article

First-Principles Study of Pt-Based Bifunctional Oxygen Evolution & Reduction Electrocatalyst: Interplay of Strain and Ligand Effects

Seung-hoon Kim [1,2], Yoonmook Kang [2,*] and Hyung Chul Ham [3,*]

[1] Center for Hydrogen and Fuel Cell Research, Korea Institute of Science and Technology (KIST), 5, Hwarangno 14-gil, Seongbuk-gu, Seoul 02792, Korea; s.kim@kist.re.kr
[2] Graduate School of Energy and Environment (KU-KIST Green School), Korea University, 145, Anan-ro, Seungbuk-gu, Seoul 02841, Korea
[3] Education and Research Center for Smart Energy and Materials, Department of Chemistry and Chemical Engineering, Inha University, 100, Inha-ro, Michuhol-gu, Incheon 22212, Korea
* Correspondence: ddang@korea.ac.kr (Y.K.); ham.hyungchul@inha.ac.kr (H.C.H.)

Abstract: We examined the oxygen evolution reaction (OER) and oxygen reduction reaction (ORR) of Pt-based Pt_3M/Pt nanoalloy catalysts (where M represents a 3d transition metal) for bifunctional electrocatalysts using spin-polarized density functional theory calculations. First, the stability of the Pt_3M/Pt catalyst was investigated by calculating the bulk formation energy and surface separation energy. Using the calculated adsorption energies for the OER/ORR intermediates in the modeled catalysts, we predicted the OER/ORR overpotentials and potential limiting steps for each catalyst. The origins of the enhanced catalytic reactivity in Pt_3M/Pt catalysts caused by strain and ligand effects are explained separately. In addition, compared to Pt(111), the OER and ORR activities in a Pt_3Ni/Pt_{skin} catalyst with a Pt skin layer were increased by 13.7% and 18.4%, respectively, due to the strain and ligand effects. It was confirmed that compressive strain and ligand effects are key factors in improving the catalytic performance of OER/ORR bifunctional catalysts.

Keywords: electrocatalyst; oxygen evolution reaction; oxygen reduction reaction; bifunctional; density functional theory

Citation: Kim, S.-h.; Kang, Y.; Ham, H.C. First-Principles Study of Pt-Based Bifunctional Oxygen Evolution & Reduction Electrocatalyst: Interplay of Strain and Ligand Effects. *Energies* **2021**, *14*, 7814. https://doi.org/10.3390/en14227814

Academic Editor: Giorgio Vilardi

Received: 23 October 2021
Accepted: 19 November 2021
Published: 22 November 2021

1. Introduction

To achieve a clean and sustainable future, green energy technologies, such as hydrogen fuel cells and metal–air batteries, have been attracting significant attention since they can be expected to utilize renewable energy and reduce energy consumption [1–3]. Among these technologies, one of the core elements is an oxygen electrode that electrochemically oxidizes water via oxygen evolution reaction (OER) or reduces oxygen via oxygen reduction reaction (ORR) [4]. To overcome the low kinetics of these two reactions, Ir- and Ru-based noble metal catalysts are mainly used for OER, and Pt-based catalysts are used for ORR [5–9].

A bifunctional catalyst applied to a unitized reversible fuel cell (URFC) should have excellent activity in both OER and ORR. Most URFCs are based on proton exchange membranes, and hydrogen and oxygen are used as the fuel. URFC has two operating modes: electrolysis mode and fuel cell mode. In the electrolysis mode, water is oxidized through OER of an oxygen electrode, giving protons and electrons and releasing oxygen [$2H_2O \rightarrow 2O_2 + 4H^+ + 4e^-$]. These protons and electrons are transferred to the hydrogen electrode via the membrane and electric potential, respectively. In the hydrogen electrode, hydrogen is produced by a hydrogen evolution reaction (HER) in which four protons are combined with four electrons [$4H^+ + 4e^- \rightarrow 2H_2$]. Overall, in this process, water is decomposed into hydrogen and oxygen by an electric potential. Among both OER and HER, OER is a limited process due to its relatively higher overpotential.

On the other hand, in fuel cell mode, hydrogen and oxygen are injected to a hydrogen electrode and oxygen electrode, respectively. The electrode that generated hydrogen during the electrolysis mode oxidizes the injected hydrogen and splits it into protons and electrons [$2H_2 \rightarrow 4H^+ + 4e^-$] via the hydrogen oxidation reaction (HOR). Likewise, the electrode that oxidized water during electrolysis mode reduces the injected oxygen to produce water [$2O_2 + 4H^+ + 4e^- \rightarrow 2H_2O$] via ORR. Of the two reactions, ORR is a limiting process.

The known ORR and OER catalysts so far show good activity only in their respective reactions [10–12]. Developing low-cost, stable bifunctional electrocatalysts, especially those having excellent activity for both OER and ORR, remains a major scientific and technological challenge [13–15].

One way to improve catalytic activity and reduce costs is by lowering the noble metal content through alloying, in which two or more guest atoms are introduced and mixed into an existing metal catalyst [16–18]. By alloying, the catalytic properties, such as the core structure, lattice distance, chemical properties of the surface, chemical composition of the ensemble, and surface atomic coordination, are changed, which greatly affects the activity and stability of the catalysts [19]. Among these property changes, the three factors that have the greatest influence are (1) strain effect (change in the lattice distance of the core), (2) ligand effect (change in chemical properties of the atoms on the surface), and (3) ensemble effect (change in catalytic properties of an ensemble of atoms on the surface) [20–23]. In actual alloy catalysts, these three effects appear mixed together, making it difficult to distinguish them separately. However, it is possible to clearly examine each effect using first-principles investigations, and it can provide insight to other researchers because the origin of the enhanced reactivity can be apparently identified.

In this study, electrochemical OER and ORR on Pt-based alloy catalysts were investigated through first-principles calculations based on density functional theory (DFT). In core-shell Pt_3M/Pt catalysts made of Pt and an alloy with M, the strain and ligand effect on the activity of both OER/ORR were investigated. We found that the Pt_3Ni/Pt_{skin} catalyst with a Pt skin-layer showed OER and ORR activities enhanced by 13.7% and 18.4%, respectively, compared to the Pt(111) catalyst due to strain and ligand effects.

2. Computational Details

All first-principles calculations were performed based on spin-polarized DFT, as implemented in the Vienna Ab-initio Simulation Package (VASP) [24–26]. The projector augmented wave (PAW) method using a plane wave basis set was implemented to describe the interaction between the core and valence electrons [27]. The Perdew–Burke–Ernzerhof (PBE) exchange–correlation functional within a generalized gradient approximation (GGA) was employed [28]. An energy cutoff of 400 eV was used for the plane-wave expansion of the electronic eigenfunctions.

To model the Pt_3M/Pt catalysts, we first built an fcc-structured Pt bulk unit cell with lattice parameters optimized with a = 3.97 Å, which is close to the experimental result of 3.92 Å [29]. Using this unit cell, we prepared fcc-structured Pt_3M bulk unit cells by replacing one of the Pt atoms with M (where M represents a 3d transition metal). We also examined the thermodynamic feasibility of Pt_3M alloy formation by calculating the bulk formation energy of Pt_3M:

$$\Delta E_{Bulk} = [E_{Pt3M} - (N_{Pt}E_{Pt} + N_M E_M)]/(N_{Pt3} + N_{M1})$$

where E_{Pt3M}, E_{Pt}, E_M, N_{Pt}, N_M, N_{Pt3}, and N_{M1} represent the total energies of the bulk Pt_3M, bulk Pt, bulk M and the number of atoms in bulk Pt and bulk M, the number of Pt atoms in bulk Pt_3M, and the number of M atoms in bulk Pt_3M, respectively.

To separately examine the strain and ligand effects caused by Pt_3M alloying, we prepared (2×2) Pt_3M/Pt (tri-layered Pt supported on $Pt_3M(111)$ alloy substrate) and Pt_3M/Pt_{skin} (the mono-layered Pt on the $Pt_3M(111)$ alloy substrate) slab models with five atomic layers, each containing four atoms, as shown in Figure 1. We also investigated the OER/ORR on a Pt(111) (pure Pt single-crystal surface) slab model as a reference. By

comparing Pt(111) and Pt_3M/Pt, it can be seen that the strain effect changes the characteristics of Pt(111) catalysts, and the difference between Pt_3M/Pt and Pt_3M/Pt_{skin} can be seen as a change caused by the ligand effect. This is due to the fact that, in previous studies, we found that the change in the surface electronic structure due to the ligand effect was neglected when the shell thickness was above three atomic layers [30,31]. These slab models were isolated from periodic images in the vertical z direction by a vacuum space corresponding to eight atomic layers. The bottom two layers were fixed at corresponding bulk positions, while the upper three layers were fully relaxed using the conjugate gradient method until the residual forces on all constituent atoms became smaller than 5×10^{-2} eV/Å [32]. For the Brillouin zone integration, we accepted ($16 \times 16 \times 16$) and ($5 \times 5 \times 1$) Monkhorst-Pack meshes of k-points to obtain the optimal geometries and total energies of the bulk and slab models [33]. To calculate the surface electronic structure, we doubled the mesh to ($10 \times 10 \times 1$).

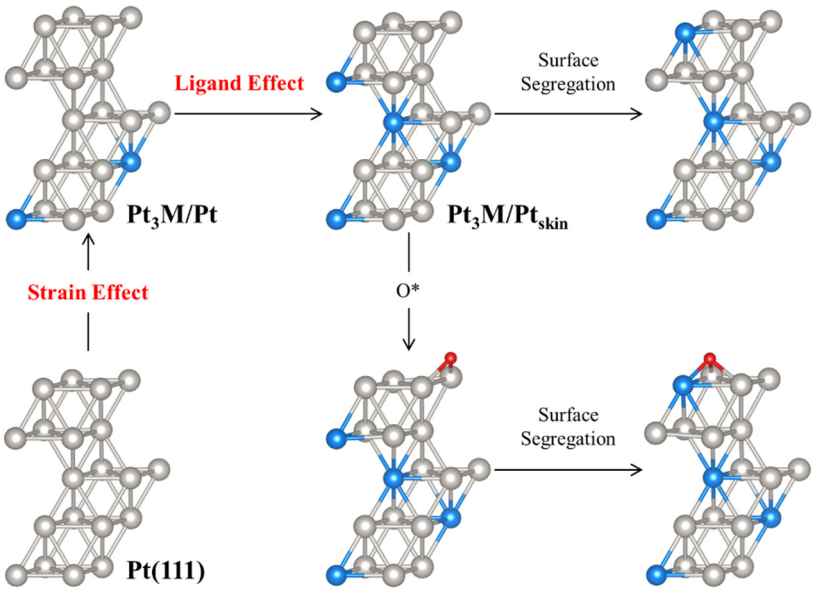

Figure 1. DFT slab models. Gray, blue, and red spheres represent Pt, M, and O atoms, respectively. An asterisk (*) denotes the adsorption state.

The d-band occupancy near the Fermi level (χ_F) was calculated as the ratio of the area of partial density of state (PDOS) corresponding to the "near Fermi level" (-0.25 eV $< E - E_F <$ 0.25 eV) to the total area of PDOS:

$$\chi_F = \frac{\int_{-0.25}^{+0.25} \rho d\varepsilon}{\int_{-\infty}^{\infty} \rho d\varepsilon}$$

where ρ and ε represent the electron density and energy level, respectively. The charge density of the surface Pt atoms (σ) was estimated by Bader charge analysis with a special convergence test over a charge density grid [34].

The adsorption energy of the OER/ORR intermediates (ΔE_{Ads} (X), X:O, OH, and OOH) was calculated using the following equation:

$$\Delta E_{Ads}\,(X) = E_{bare} + E_X - E_{X^*}$$

where E_{bare}, E_X, and E_{X^*} represent the total energy of the bare slab, isolated X molecule in the gas phase, and the slab with X adsorbed, respectively (an asterisk * denotes the adsorption state).

To examine the surface stability of the Pt_3M/Pt_{skin} models, we calculated the surface segregation energy of M under pristine (ΔE_{Seg}) and oxygen-rich (ΔE_{Seg_O}) conditions:

$$\Delta E_{Seg} = E_{AS} - E_{bare}$$

$$\Delta E_{Seg\_O} = E_{AS\_O} - E_{O^*}$$

where E_{AS}, E_{AS_O}, and E_{O^*} represent the total energies of the Pt_3M/Pt_{skin} slab after segregation, with O adsorbed after segregation, and with O adsorbed, respectively.

To calculate the Gibbs free energy change (ΔG) of every step for OER/ORR, we introduced a computational hydrogen electrode (CHE) model, as pioneered by Nørskov [35]. In this model, the free energy of a coupled proton and electron is equivalent to that of half gaseous H_2 [$G(H^+ + e^-) = {}^1/_2\, G(H_2)$] under standard reaction conditions (T = 298.15 K, P = 1 bar, pH = 0) with no external potential. We obtained the ΔG value using the following method:

$$\Delta G = \Delta E - T\Delta S + \Delta ZPE - neU$$

where ΔE, ΔS, ΔZPE, n, and U are the difference in total energies directly obtained from DFT calculations, difference in entropies, difference in zero-point energies, number of transferred electrons during the reaction, and operating potential in CHE, respectively. The entropies and zero-point energies of the OER/ORR intermediates were calculated using the vibrational frequencies, in which the adsorption vibrational mode was calculated explicitly with all atoms fixed except for the OER/ORR intermediates [36]. The entropy values of the adsorbates under the reaction conditions were taken from the NIST Chemistry WebBook [37]. We also included the solvation effect by the electrochemical double layer (EDL). For OH* and OOH*, constant bilayer correction was introduced to stabilize the Gibbs free energy by 0.5 and 0.25 eV, respectively [35].

3. Results and Discussions

3.1. Structural Stability of Pt_3M/Pt Catalysts

To elucidate the thermodynamic stability of bulk Pt_3M alloy, we calculated the bulk formation energy (ΔE_{Bulk}) of Pt_3M from pure Pt and M metals, as shown in Table 1. We found that ΔE_{Bulk} values for all Pt_3M were negative, indicating that Pt_3M alloying from Pt and 3d transition metals is a thermodynamically feasible process. We also found that the lattice distance in bulk Pt_3M is reduced from 3.87 Å to 3.94 Å compared to Pt (3.97 Å), while that of Pt_3Sc is increased to 4.00 Å. These values indicate that compared to pure Pt(111) surfaces, the Pt_3M alloy catalyst is subjected to compressive (−) and tensile (+) strains from −2.44% to +0.73% in the direction parallel to the surface. Many theoretical and experimental studies have revealed that compressive strain induces weak adsorption of reaction intermediates, and tensile strain is the opposite [20,21,38]. Based on these results, we could expect that relatively weak adsorption of the OER/ORR intermediates would occur on the Pt_3M/Pt catalysts, except for the Pt_3Sc/Pt case.

Table 1. Calculated lattice parameters, bulk formation energy, and segregation energy with and without oxygen species.

	α (Å)	**ΔE_{Bulk} (eV/Atom)**	**ΔE_{Seg} (eV)**	**ΔE_{Seg_O} (eV)**
Pt_3Sc	4.00	−1.05	1.05	−0.02
Pt_3Ti	3.94	−0.84	1.20	−0.21
Pt_3V	3.92	−0.43	0.96	−0.99
Pt_3Cr	3.91	−0.25	0.86	−0.28
Pt_3Mn	3.92	−0.39	0.89	0.15
Pt_3Fe	3.91	−0.20	0.89	0.11
Pt_3Co	3.88	−0.06	0.74	0.01
Pt_3Ni	3.87	−0.07	0.74	0.04
Pt_3Cu	3.89	−0.11	0.70	0.25

Under OER/ORR conditions, 3d transition metals exposed to the surface may be eluted into the acidic solution, and oxygen species such as O and OH in aqueous solution can affect the stability of the catalytic surface. To elucidate the surface stability of the Pt_3M/Pt_{skin} catalysts, we calculated the surface segregation energy (ΔE_{Seg} and ΔE_{Seg_O}) of M from the sub-surface (second layer from top) to the topmost surface with and without oxygen species. As shown in Table 1, all ΔE_{Seg} values were calculated to be positive, indicating that the segregation process of sub-surface M atoms to the topmost surfaces under vacuum conditions is thermodynamically unstable. However, the surface segregation energy (ΔE_{Seg_O}) is reduced in the presence of oxygen species. Moreover, Pt_3Sc/Pt_{skin}, Pt_3Ti/Pt_{skin}, Pt_3V/Pt_{skin}, and Pt_3Cr/Pt_{skin} showed negative ΔE_{Seg_O} values, indicating that these four catalysts are unstable because the 3d transition metals inside the sub-surface can be eluted by surface oxygen species. Therefore, we excluded the above four catalysts with a Pt skin-layer from further OER/ORR investigation.

3.2. OER/ORR Mechanism and Reaction Energetics

Several authors have suggested that oxygen reduction and evolution on Pt surfaces follow four electron pathways (known as an associative mechanism) in acidic media, and we also considered associative OER/ORR in this study [6,8,9,12,14]. The elementary steps are as follows:

Figure 2 displays the OER/ORR Gibbs free energy diagram for the Pt(111) catalyst. In OER on Pt(111), only the step from O* to OH* is endothermic, and the energy difference between them is the overpotential (η_{OER}). To minimize η_{OER}, O* should be less stabilized, and OH* should be more stabilized. In other words, the weaker the O adsorption and the stronger the OH adsorption, the more active the OER. On the contrary, the OOH adsorption is not directly related to OER activity.

$$* + H_2O \leftrightarrow OH^* + (H^+ + e^-)$$

$$OH^* \leftrightarrow O^* + (H^+ + e^-)$$

$$O^* + H_2O \leftrightarrow OOH^* + (H^+ + e^-)$$

$$OOH^* \leftrightarrow O_2 + (H^+ + e^-)$$

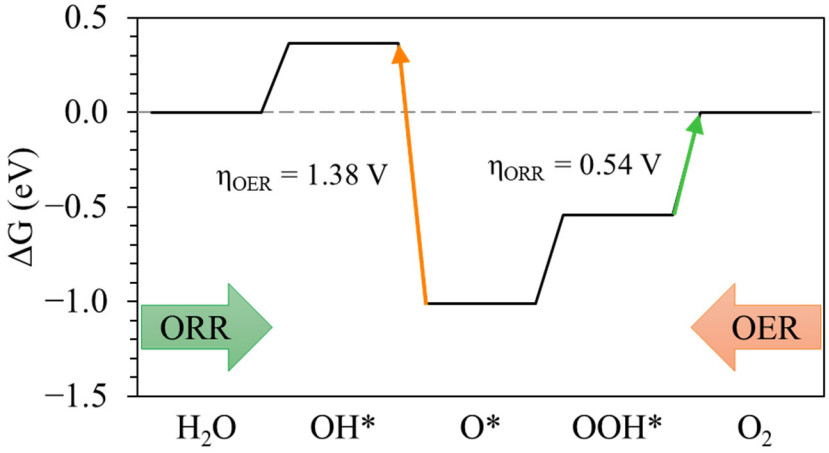

Figure 2. OER/ORR Gibbs free energy diagram of Pt(111) catalyst at equilibrium potential (U = 1.23 V) under acidic conditions (pH = 0 and T = 298 K) An asterisk (*) denotes the adsorption state.

In the case of ORR, the potential determining step (PDS) was found to be the formation of O_2 from OOH*, and the weaker the OOH adsorption, the more active the ORR. However, the PDS can be shifted as the adsorption energies of O, OH, and OOH change.

In ORR catalysis, it is important to find a catalyst with moderate adsorption of these three reaction intermediates.

Table 2 lists the OER and ORR overpotentials for each catalyst. All of the Pt_3M/Pt and Pt_3M/Pt_{skin} catalysts showed a reduced OER overpotential compared to the Pt(111) catalyst, except in the Pt_3Sc/Pt case. In the case of ORR activity, it was found that the overpotentials of the modeled catalysts, except for Pt_3Sc/Pt, Pt_3Ti/Pt, Pt_3Mn/Pt, and Pt_3Cu/Pt, were reduced compared to that of the Pt(111) catalyst. With the overpotential gap (ΔG_{Gap}), an indicator of the OER/ORR bifunctional activity obtained by the sum of two overpotentials, it was also found that all catalysts showed a reduced overpotential gap compared to Pt(111), except for Pt_3Sc/Pt and Pt_3Ti/Pt. Among all the cases, Pt_3Ni/Pt_{skin} had the lowest overpotential gap and increased OER and ORR activity by 13.7% and 18.4%, respectively.

Table 2. Calculated overpotentials for OER and ORR in Pt(111), Pt_3M/Pt, and Pt_3M/Pt_{skin} catalysts. ΔG_{Gap} is the sum of two overpotentials representing activity of OER/ORR bifunctional catalyst.

	η_{OER} (V)	η_{OER} (V)	ΔG_{Gap} (eV)
Pt(111)	1.38	0.54	1.92
Pt_3Sc/Pt	1.46	0.74	2.20
Pt_3Ti/Pt	1.35	0.59	1.94
Pt_3V/Pt	1.29	0.52	1.81
Pt_3Cr/Pt	1.28	0.50	1.79
Pt_3Mn/Pt	1.32	0.59	1.91
Pt_3Fe/Pt	1.31	0.54	1.85
Pt_3Co/Pt	1.24	0.50	1.74
Pt_3Ni/Pt	1.21	0.53	1.73
Pt_3Cu/Pt	1.26	0.58	1.84
Pt_3Mn/Pt_{skin}	1.23	0.46	1.68
Pt_3Fe/Pt_{skin}	1.21	0.52	1.73
Pt_3Co/Pt_{skin}	1.15	0.47	1.63
Pt_3Ni/Pt_{skin}	1.12	0.47	1.59
Pt_3Cu/Pt_{skin}	1.11	0.50	1.62

3.3. Origin of Enhanced OER/ORR Activity on Pt_3M/Pt Catalysts

To better understand the relationship between the OER/ORR activity and adsorption energy of the reaction intermediates, we display the adsorption energies of O and OH, and the changes in OER/ORR overpotentials in Figure 3. As mentioned earlier, the OER activity increased with weaker O adsorption and stronger OH adsorption. This is because the PDS of OER is the OH* formation step from O*, as is clearly revealed in Figure 3a.

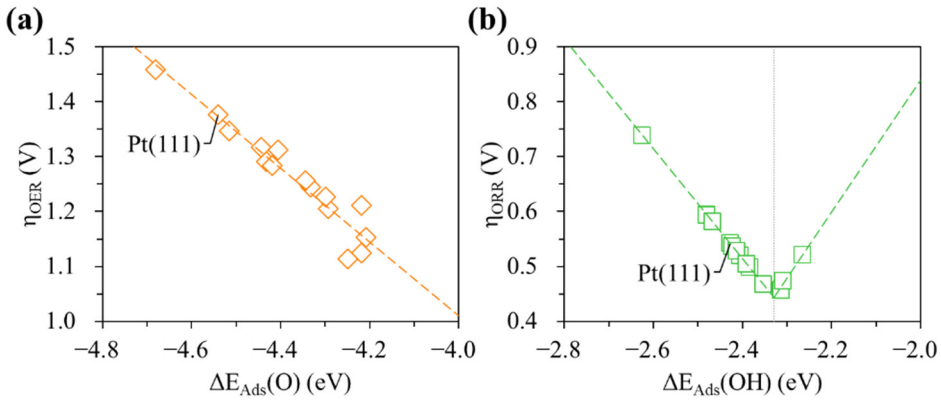

Figure 3. Relation between OER/ORR overpotential and adsorption energy of reaction intermediates O (**a**) and OH (**b**). A smaller negative value on the *x*-axis (to the right) indicates weaker adsorption.

Meanwhile, we found that the ORR overpotential decreased until ΔE_{Ads} (OH) reached −2.23 eV, and then it increased again as the adsorption weakened, as shown in Figure 3b. This was due to the shift of PDS from [OOH* → O_2] to [H_2O → OH*].

To clearly understand the reasons for the change in the adsorption energy of the OER/ORR intermediates, the lattice strain and adsorption energy are shown in Figure 4. It can be clearly seen that monoatomic O species adsorbed weaker with stronger compressive strain, whereas OH adsorption had no clear relationship with strain change. Based on these results, we confirmed that the enhanced OER activity of the Pt_3M/Pt catalyst was mainly due to weak O adsorption resulting from the compressive strain. We also found that compressive strain did not significantly affect the OH adsorption energy. Therefore, it is not directly related to the ORR activity.

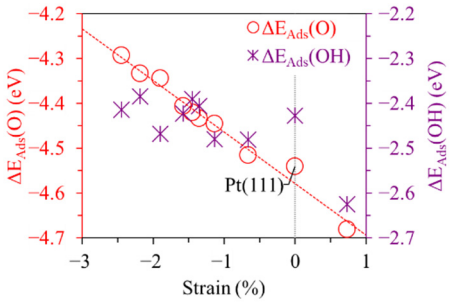

Figure 4. Changes in adsorption energy of OER/ORR intermediates due to the strain effect.

We further investigated how the ligand effect affects OER/ORR activity by comparing the O and OH adsorption energies of the Pt_3M/Pt and Pt_3M/Pt_{skin} catalysts. For all Pt_3M/Pt (M: Mn, Fe, Co, Ni, and Cu), the ΔE_{Ads} (O) values shifted less negatively from [−4.44 eV (Mn), −4.41 eV (Fe), −4.33 eV (Co), −4.29 eV (Ni), and −4.34 eV (Cu)] to [−4.30 eV (Mn), −4.22 eV (Fe), −4.21 eV (Co), −4.22 eV (Ni), and −4.25 eV (Cu)] as the ligand effect was added, and this trend was also found in OH adsorption. This indicates that the ligand effect alters the surface electronic structure to be less active and, in turn, enhances the OER/ORR activity.

To better understand the origin of the enhanced activity, we calculated the surface electronic structure. In Figure 5a, we plot the partial density of states (PDOS) of surface Pt. The PDOS shapes of the catalytic surfaces of Pt_3Ni/Pt and Pt_3Ni/Pt_{skin} are similar to that of Pt(111). However, near the Fermi level ($E - E_F \approx 0$ eV), we found that the PDOS on the Pt_3Ni/Pt surface was slightly reduced compared to the Pt(111) catalysts, and the PDOS level of Pt_3Ni/Pt_{skin} was clearly reduced compared to the Pt(111) and Pt_3Ni/Pt catalysts.

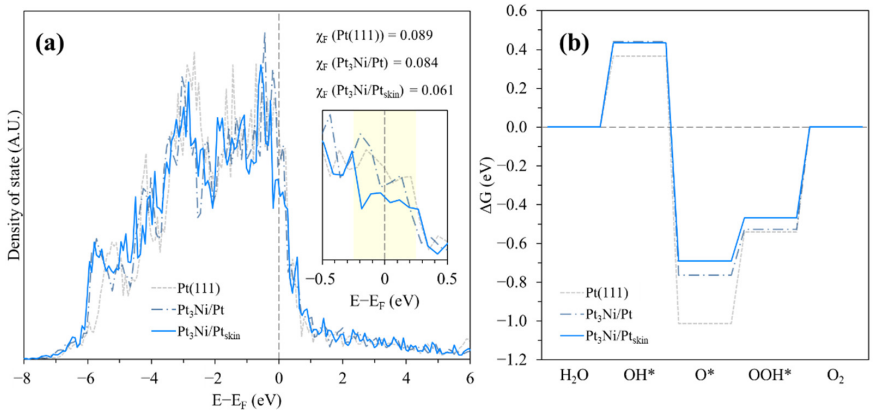

Figure 5. (**a**) PDOS of the surface Pt atoms, and (**b**) OER/ORR Gibbs free energy diagram at equilibrium potential for Pt(111), Pt_3Ni/Pt, and Pt_3Ni/Pt_{skin} catalysts. An asterisk (*) denotes the adsorption state.

According to the d-band theory, the lower the electron density on the surface of the catalyst near the Fermi level, the weaker the adsorption with the adsorbate. This is due to the fact that electrons near the Fermi level migrate to the adsorbate during bond formation [39–41]. Our calculation results revealed that the d-band occupancy near the Fermi level (χ_F) is reduced by strain and ligand effects and, in particular, the ligand effect significantly reduces the electron density near the Fermi level [χ_F(Pt(111) = 0.089 $\rightarrow$ χ_F(Pt_3Ni/Pt) = 0.084 $\rightarrow$ χ_F(Pt_3Ni/Pt_{skin}) = 0.061)]. In contrast, the total surface charge density (σ) calculated by Bader charge analysis was almost the same for all three catalysts [σ(Pt(111) = 10.05, σ(Pt_3Ni/Pt) = 10.04, σ(Pt_3Ni/Pt_{skin} = 10.08]. This indicates that some of the active electrons near the Fermi energy level participating in the bond shift to the inactive state, while the total electron density on the catalytic surface barely changed. As a result, in the Pt_3Ni/Pt_{skin} catalyst with a Pt skin-layer, the adsorption energies of the OER/ORR intermediates were adjusted to an appropriate level due to the change in surface electron density by compressive strain and ligand effects, which was revealed as a 17% reduced OER/ORR overpotential gap compared to the Pt(111) catalyst as shown in Figure 5b.

4. Conclusions

In this study, using first-principles computation based on spin-polarized DFT, we investigated electrochemical OER and ORR on Pt-based Pt_3M alloy catalysts, and we decoupled the strain and ligand effects by comparing Pt(111), Pt_3M/Pt, and Pt_3M/Pt_{skin} models.

First, we examined the structural stability of Pt_3M/Pt and Pt_3M/Pt_{skin} catalysts by calculating bulk formation energy and surface segregation energy, showing that the formation of all Pt_3M alloys is thermodynamically feasible. However, Pt skin-layered Pt_3Sc/Pt_{skin}, Pt_3Ti/Pt_{skin}, Pt_3V/Pt_{skin}, and Pt_3Cr/Pt_{skin} are unstable in reaction conditions.

Second, compared to the Pt(111) catalyst, our DFT calculations predicted reduced OER and ORR overpotentials for most Pt_3M/Pt and Pt_3M/Pt_{skin} catalysts due to the weaker O adsorption and moderate OH adsorption.

Finally, by electronic structure calculations, we found that the origin of the change in adsorption energy of OER/ORR intermediates is the reduced electron density near the Fermi level caused by compressive strain and ligand effects. Among all the catalysts, Pt_3Ni/Pt_{skin} showed the lowest overpotential gap, which was reduced by 17% compared to Pt(111).

Our theoretical study identified that Pt-based alloy catalyst can show improved performance even in the reverse reaction of OER, and it provides a fundamental understanding of electrochemical OER and ORR catalysis for researchers developing bifunctional oxygen electrodes, especially regarding the interplay of strain and ligand effects on the alloy catalysts, and it will help advance a clean and sustainable future. However, this study focused on the origins of enhanced OER/ORR activity due to strain and ligand effects and did not address catalytic durability. This will be further explored in the next study.

Author Contributions: Conceptualization, investigation, and writing, S.-h.K.; funding acquisition, Y.K.; supervision, H.C.H. All authors have read and agreed to the published version of the manuscript.

Funding: This work was supported by the National Research Foundation of Korea grants (grant nos. NRF-2021M3I3A1084813) funded by the Ministry of Science and ICT of the Korean Government. This work was also supported by the Korea Institute of Planning and Evaluation for Technology in Food, Agriculture and Forestry(IPET) through the Smart Farm Innovation Technology Development Program, funded by the Ministry of Agriculture, Food and Rural Affairs(MAFRA), Ministry of Science and ICT(MSIT), Rural Development Administration(RDA) (421036031HD020).

Conflicts of Interest: The authors declare no conflict of interest.

References

1. Pivovar, B. Catalysts for fuel cell transportation and hydrogen related uses. *Nat. Catal.* **2019**, *2*, 562–565. [CrossRef]
2. Jiao, Y.; Zheng, Y.; Jaroniec, M.; Qiao, S.Z. Design of electrocatalysts for oxygen- and hydrogen-involving energy conversion reactions. *Chem. Soc. Rev.* **2015**, *44*, 2060–2086. [CrossRef] [PubMed]
3. Seh, Z.W.; Kibsgaard, J.; Dickens, C.F.; Chorkendorff, I.; Nørskov, J.K.; Jaramillo, T.F. Combining theory and experiment in electrocatalysis: Insights into materials design. *Science* **2017**, *355*, 146. [CrossRef]
4. Kan, D.; Wang, D.; Zhang, X.; Lian, R.; Xu, J.; Chen, G.; Wei, Y. Rational design of bifunctional ORR/OER catalysts based on Pt/Pd-doped Nb2CT2 MXene by first-principles calculations. *J. Mater. Chem. A* **2020**, *8*, 3097–3108. [CrossRef]
5. Kim, Y.J.; Lim, A.; Kim, J.M.; Lim, D.; Chae, K.H.; Cho, E.N.; Han, H.J.; Jeon, K.U.; Kim, M.; Lee, G.H.; et al. Highly efficient oxygen evolution reaction via facile bubble transport realized by three-dimensionally stack-printed catalysts. *Nat. Commun.* **2020**, *11*, 4921. [CrossRef] [PubMed]
6. Naito, T.; Shinagawa, T.; Nishimoto, T.; Takanabe, K. Recent advances in understanding oxygen evolution reaction mechanisms over iridium oxide. *Inorg. Chem. Front.* **2021**, *8*, 2900–2917. [CrossRef]
7. Qu, H.-Y.; He, X.; Wang, Y.; Hou, S. Electrocatalysis for the Oxygen Evolution Reaction in Acidic Media: Progress and Challenges. *Appl. Sci.* **2021**, *11*, 4320. [CrossRef]
8. Reier, T.; Oezaslan, M.; Strasser, P. Electrocatalytic Oxygen Evolution Reaction (OER) on Ru, Ir, and Pt Catalysts: A Comparative Study of Nanoparticles and Bulk Materials. *ACS Catal.* **2012**, *2*, 1765–1772. [CrossRef]
9. Wang, J.; Zhao, C.-X.; Liu, J.-N.; Ren, D.; Li, B.-Q.; Huang, J.-Q.; Zhang, Q. Quantitative kinetic analysis on oxygen reduction reaction: A perspective. *Nano Mater. Sci.* **2021**, *3*, 313–318. [CrossRef]
10. Sui, S.; Wang, X.; Zhou, X.; Su, Y.; Riffat, S.; Liu, C. A comprehensive review of Pt electrocatalysts for the oxygen reduction reaction: Nanostructure, activity, mechanism and carbon support in PEM fuel cells. *J. Mater. Chem. A* **2017**, *5*, 1808–1825. [CrossRef]
11. Li, Y.; Lu, J. Metal–Air Batteries: Will They Be the Future Electrochemical Energy Storage Device of Choice? *ACS Energy Lett.* **2017**, *2*, 1370–1377. [CrossRef]
12. Tian, X.T.; Lu, X.F.; Xia, B.Y.; Lou, X.W. Advanced Electrocatalysts for the Oxygen Reduction Reaction in Energy Conversion Technologies. *Joule* **2020**, *4*, 45–68. [CrossRef]
13. Rai, V.; Lee, K.P.; Safanama, D.; Adams, S.; Blackwood, D.J. Oxygen Reduction and Evolution Reaction (ORR and OER) Bifunctional Electrocatalyst Operating in a Wide pH Range for Cathodic Application in Li–Air Batteries. *ACS Appl. Energy Mater.* **2020**, *3*, 9417–9427. [CrossRef]
14. Wu, X.; Tang, C.; Cheng, Y.; Min, X.; Jiang, S.P.; Wang, S. Bifunctional Catalysts for Reversible Oxygen Evolution Reaction and Oxygen Reduction Reaction. *Chem. A Eur. J.* **2020**, *26*, 3906–3929.
15. Liu, Z.; Zhao, Z.; Peng, B.; Duan, X.; Huang, Y. Beyond Extended Surfaces: Understanding the Oxygen Reduction Reaction on Nanocatalysts. *J. Am. Chem. Soc.* **2020**, *142*, 17812–17827. [CrossRef] [PubMed]
16. Liu, P.; Nørskov, J.K. Ligand and ensemble effects in adsorption on alloy surfaces. *Phys. Chem. Chem. Phys.* **2001**, *3*, 3814–3818. [CrossRef]
17. Wu, Z.-P.; Caracciolo, D.T.; Maswadeh, Y.; Wen, J.; Kong, Z.; Shan, S.; Vargas, J.A.; Yan, S.; Hopkins, E.; Park, K.; et al. Alloying–realloying enabled high durability for Pt–Pd-3d-transition metal nanoparticle fuel cell catalysts. *Nat. Commun.* **2021**, *12*, 859. [CrossRef]
18. Wang, Y.; Zhang, F.; Stumpf, R.; Lin, P.; Chou, M.Y. Catalytic effect of near-surface alloying on hydrogen interaction on the aluminum surface. *Phys. Rev. B* **2011**, *83*, 195419. [CrossRef]
19. Zafeiratos, S.; Piccinin, S.; Teschner, D. Alloys in catalysis: Phase separation and surface segregation phenomena in response to the reactive environment. *Catal. Sci. Technol.* **2012**, *2*, 1787–1801. [CrossRef]
20. Westsson, W.; Picken, S.; Koper, G. The effect of lattice strain on catalytic activity. *Chem. Commun.* **2019**, *55*, 1338–1341. [CrossRef]
21. Huang, H.; Jia, H.; Liu, Z.; Gao, P.; Zhao, J.; Luo, Z.; Yang, J.; Zeng, J. Understanding of Strain Effects in the Electrochemical Reduction of CO_2: Using Pd Nanostructures as an Ideal Platform. *Angew. Chem.* **2017**, *56*, 3594–3598. [CrossRef] [PubMed]
22. Bligaard, T.; Nørskov, J.K. Ligand effects in heterogeneous catalysis and electrochemistry. *Electrochim. Acta* **2007**, *52*, 5512–5516. [CrossRef]
23. Li, S.; Tian, W.; Liu, Y. The ligand effect of atomically precise gold nanoclusters in tailoring catalytic properties. *Nanoscale* **2021**, *13*, 16847–16859. [CrossRef]
24. Hohenberg, P.; Kohn, W. Inhomogeneous electron gas. *Phys. Rev.* **1964**, *136*, B864–B871. [CrossRef]
25. Kohn, W.; Sham, J. Self-consistent equations including exchange and correlation effects. *Phys. Rev.* **1965**, *140*, A1133–A1138. [CrossRef]
26. Kresse, G.; Furthmüller, J. Efficient iterative schemes for ab initio total-energy calculations using a plane-wave basis set. *Phys. Rev. B* **1996**, *124*, 11169–11186. [CrossRef] [PubMed]
27. Blöchl, P.E. Projector augmented-wave method. *Phys. Rev. B* **1994**, *50*, 17953–17979. [CrossRef]
28. Perdew, J.P.; Burke, K.; Ernzerhof, M. Generalized gradient approximation made simple. *Phys. Rev. Lett.* **1996**, *77*, 3865–3868. [CrossRef]
29. Krupski, K.; Moors, M.; Jóźwik, P.; Kobiela, T.; Krupski, A. Structure Determination of Au on Pt(111) Surface: LEED, STM and DFT Study. *Materials* **2015**, *8*, 2935–2952. [CrossRef]

30. Cho, J.; Lee, S.; Han, J.; Yoon, S.P.; Nam, S.W.; Choi, S.H.; Lee, K.-Y.; Ham, H.C. Importance of Ligand Effect in Selective Hydrogen Formation via Formic Acid Decomposition on the Bimetallic Pd/Ag Catalyst from First-Principles. *J. Phys. Chem. C* **2014**, *118*, 22553–22560. [CrossRef]
31. Lee, S.; Cho, J.; Jang, J.H.; Han, J.; Yoon, S.P.; Nam, S.W.; Lim, T.H.; Ham, H.C. Impact of d-Band Occupancy and Lattice Contraction on Selective Hydrogen Production from Formic Acid in the Bimetallic Pd3M (M = Early Transition 3d Metals) Catalysts. *ACS Catal.* **2016**, *6*, 134–142. [CrossRef]
32. Jiang, H.; Yang, W. Conjugate-gradient optimization method for orbital-free density functional calculations. *J. Chem. Phys.* **2004**, *121*, 2030–2036. [CrossRef]
33. Blöchl, P.E.; Jepsen, O.; Anderson, O.K. Improved tetrahedron method for Brillouin-zone integrations. *Phys. Rev. B* **1994**, *49*, 16223–16233. [CrossRef] [PubMed]
34. Sanville, E.; Kenny, S.D.; Smith, R.; Henkelman, G. Improved Grid-Based Algorithm for Bader Charge Allocation. *J. Comput. Chem.* **2007**, *28*, 899–908. [CrossRef] [PubMed]
35. Nørskov, J.K.; Rossmeisl, J.; Logadottir, A.; Lindqvist, L.; Kitchin, J.R.; Bligaard, T.; Jónsson, H. Origin of the overpotential for oxygen reduction at a fuel-cell cathode. *J. Phys. Chem. B* **2004**, *108*, 17886–17892. [CrossRef]
36. Skúlason, E.; Tripkovic, V.; Björketun, M.E.; Gudmundsdóttir, S.; Karlberg, G.; Rossmeisl, J.; Bligaard, T.; Jónsson, H.; Nørskov, J.K. Modeling the electrochemical hydrogen oxidation and evolution reactions on the basis of density functional theory calculations. *J. Phys. Chem. C* **2010**, *114*, 18182. [CrossRef]
37. NIST Standard Reference Database Number 69. Available online: https://webbook.nist.gov/chemistry/ (accessed on 21 November 2021).
38. Hwang, C.-K.; Kim, J.M.; Hwang, S.; Kim, J.-H.; Sung, C.H.; Moon, B.-M.; Chae, K.H.; Singh, J.P.; Kim, S.-H.; Jang, S.S.; et al. Porous Strained Pt Nanostructured Thin-Film Electrocatalysts via Dealloying for PEM Fuel Cells. *Adv. Mater. Interfaces* **2020**, *7*, 1901326. [CrossRef]
39. Nørskov, J.K.; Abild-Pedersen, F.; Studt, F.; Bligaard, T. Density functional theory in surface chemistry and catalysis. *Proc. Natl. Acad. Sci. USA* **2011**, *108*, 937–943. [CrossRef]
40. Chen, Z.W.; Chen, L.X.; Wen, Z.; Jiang, Q. Understanding electro-catalysis by using density functional theory. *Phys. Chem. Chem. Phys.* **2019**, *21*, 23782–23802. [CrossRef]
41. Bhattacharjee, S.; Waghmare, U.; Lee, S.C. An improved d-band model of the catalytic activity of magnetic transition metal surfaces. *Sci. Rep.* **2016**, *6*, 35916. [CrossRef]